

Graphene Klein tunnel transistors for high speed analog RF applications

Yaohua Tan^{1,*,\dagger}, Mirza M. Elahi^{1,\dagger}, Han-Yu Tsao¹, K. M. Masum Habib^{1,2}, N. Scott Barker¹, and Avik W. Ghosh^{1,\S}

¹Department of Electrical and Computer Engineering, University of Virginia, Charlottesville, Virginia 22904, USA

²Intel Corp., Santa Clara CA 95054, USA.

*yt5x@virginia.edu

\S ag7rq@virginia.edu

\dagger these authors contributed equally to this work

ABSTRACT

We propose Graphene Klein tunnel transistors (GKTFET) as a way to enforce current saturation while maintaining large mobility for high speed radio frequency (RF) applications. The GKTFET consists of a sequence of angled graphene p-n junctions (GPNJs). Klein tunneling creates a collimation of electrons across each GPNJ, so that the lack of substantial overlap between transmission lobes across successive junctions creates a gate-tunable transport gap without significantly compromising the on-current. Electron scattering at the device edge tends to bleed parasitic states into the gap, but the resulting pseudogap is still sufficient to create a saturated output ($I_D - V_D$) characteristic and a high output resistance. The modulated density of states generates a higher transconductance (g_m) and unity current gain cut-off frequency (f_T) than GFETs. More significantly the high output resistance makes the unity power gain cut-off frequency (f_{max}) of GKTFETs considerably larger than GFETs, making analog GKTFET potentially useful for RF electronics. Our estimation shows the f_T/f_{max} of a GKTFET with 1 μm channel reaches 33 GHz/17 GHz, and scale up to 350 GHz/53 GHz for 100 nm channel (assuming a single, scalable trapezoidal gate). The f_{max} of a GKTFET is 10 times higher than a GFET with the same channel length.

1 Introduction

Graphene-based devices have long promised exciting applications, from interconnects and transparent electrodes to gas sensing. However, their gaplessness compromises our ability to gate these devices as an efficient electronic switch. For instance, graphene is a promising channel material for radio frequency (RF) applications¹⁻⁴ due to its intrinsic high carrier mobility and long mean free path⁵⁻⁸. In fact, graphene RF devices have been reported to achieve f_T 's larger than 300 GHz for sub-100 nm channels^{9,10}. However, the gaplessness of graphene makes its output resistance low, arising from the lack of any current saturation. Consequently, the power gain cut-off frequency f_{max} of most of the reported GFETs are much lower than their f_T , and does not scale with channel length¹⁻³ (Fig 4 (f)) because of the non-scalability of the dominant contact resistances.

Efforts to improve the f_{max} of GFETs have focused on reducing the input resistance and introducing current saturation. Recent work by Guo *et al.*¹¹ showed an improved f_{max} in GFETs by significantly reducing the gate resistance using a T-shaped gate. To obtain current saturation in GFETs, an energy bandgap can in principle be introduced in graphene, such as by applying symmetry breaking strain¹² or using quantum confinement in graphene nanoribbons and nanotubes¹³. Furthermore, scattering process in a long graphene channel can also introduce natural current saturation¹⁴. However, those band gap opening mechanisms significantly reduce the carrier mobility due to the distorted bandstructure or carrier scattering events¹⁵. Thus a technique which introduces a transport gap in graphene without degrading the carrier mobility^{16,17} would be quite unique and highly desirable for graphene-based RF applications.

Over several publications in the past, we have proposed an alternative way of introducing gaps into graphene, through the employment of p-n junctions as collimator-filter pairs. A GPNJ is an angle dependent momentum filter driven by the Klein tunneling of Dirac electrons¹⁸⁻²². As a result, the GPNJ creates gate-tunable transmission gaps instead of energy band gaps, so that states are available for conduction in the ON state but removed for the OFF state. The underlying physics of Klein tunneling in tilted GPNJ has been demonstrated not only by experiments²³, but also by theoretical calculations using quasi-analytical model¹⁷, numerical models using semiclassical ray tracing²⁴, and fully quantum NEGF¹⁷. Multiple papers in the past have suggested using the GKTFET as a digital switch^{16,17,25,26}. Initial calculations¹⁶ treating the angled junctions as independent transmitters estimated ultrahigh ON-OFF ratios in excess of 10^4 , while the gate tunability of the transport gap predicted a subthreshold swing that beats the fundamental Boltzmann limit. However, in practice the ON-OFF ratio of these

devices is seen to be compromised by recurrent momentum scattering of rejected electrons at the device edges, which typically redirects leakage states into the transmission gap and limits the experimentally measured ON-OFF ratio to anywhere between 1.3²⁷ to 12. In other words, the predicted gap readily turns into a pseudogap because of parasitic scattering events.

In this work, we propose to use the pseudogap in GKTFETs for RF applications to overcome the lack of current saturation in traditional GFETs. To understand the characteristics of GKTFETs, we performed semiclassical ray tracing calculations coupled with analytical models for Klein tunneling to model electron transport in GKTFETs²⁸. The critical device parameters for a given geometry are extracted from finite element electrostatic calculations in order to estimate the cut off frequencies. According to our calculations, we argue that even a pseudogap suffices to allow GKTFETs to have distinct current saturation²⁴ and considerably larger output resistance r_0 than conventional GFETs, in fact, in excess of their contact resistances. In the process, the mobility in a GKTFET is not significantly degraded because the transmission gap dominates only for the OFF state and is kept just small enough in the ON state to still allow saturation. We expect the GKTFET can reach a f_T of 33 GHz in a 1 μm channel device, and scale up to 350 GHz at 100 nm channel length assuming ideal single gate scaling. The f_{max} of GKTFET can reach 17 GHz in a device with a 1 μm channel and 53 GHz at 100 nm length, which is more than 10 times higher than that of GFETs at a comparable channel length. Higher f_{max} of 49 GHz (1 μm) and 158 GHz (100 nm) can be reached if the gate resistance of GKTFET can be significantly reduced by reducing the gate input resistance, such as with a T-Gate.

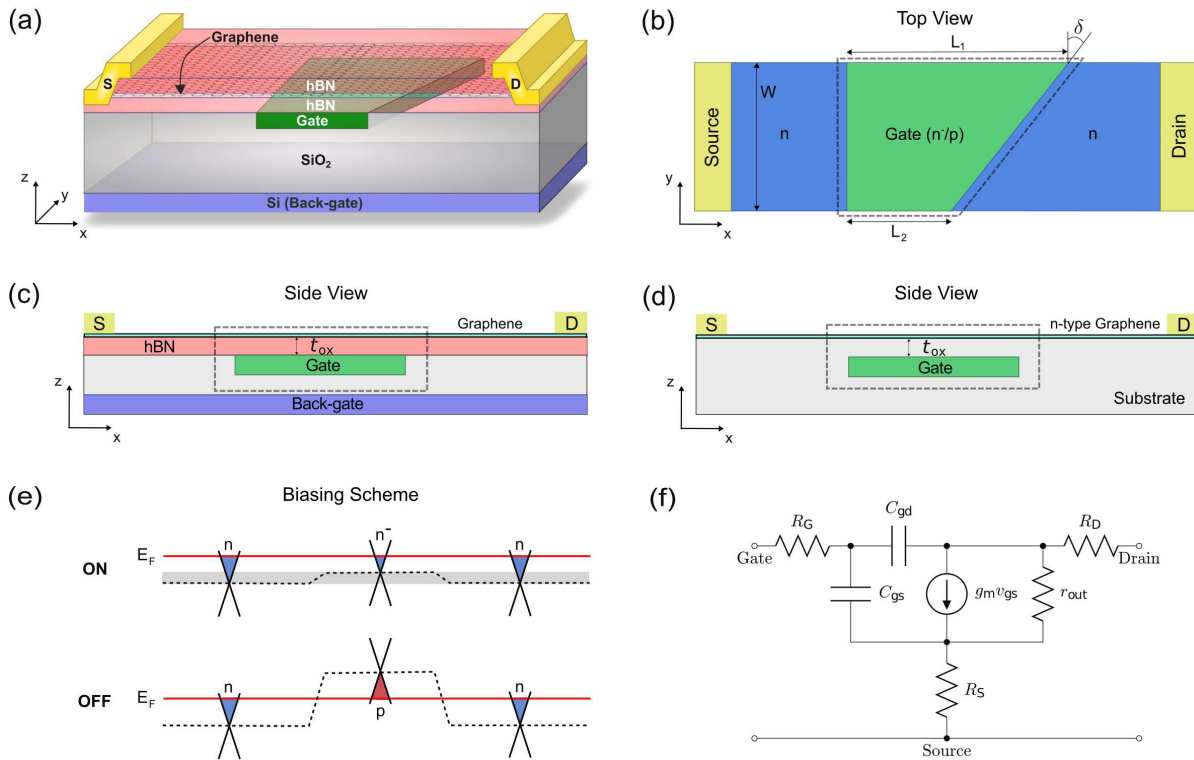


Figure 1. Klein tunnel FET based on dual tilted graphene p-n junctions (GPNJ). (a) 3D Schematic. First SiO_2 is grown on top of Si back-gate, then polysilicon/graphite wedge shaped gate (local) is deposited/stamped. A graphene flake is sandwiched between hBN and then transferred on top of SiO_2 to make sure high quality graphene is achieved⁷. (b) Top view. Gate (local) controls the charge concentration in the central green region. In the OFF state (n-p-n), two back-to-back GPNJs are formed. The left GPNJ acts as a collimator and right GPNJ acts as a filter. In the ON state (n-n⁻-n), GPNJ on the right is tilted by angle $\delta = 45^\circ$ with respect to the left one. Here we approximated the potential profile changes linearly across the junction²⁹. In this work, the device has an average gate length of $(L_1 + L_2)/2 = 1 \mu\text{m}$ ($L_1 = 1.5 \mu\text{m}$, $L_2 = 0.5 \mu\text{m}$) and a width of $W = 1 \mu\text{m}$. Gate dielectric is equivalent to 5 nm SiO_2 (EOT = 5 nm). (c) Side view for electrostatic doping by gate. (d) Side view for chemical doping case where back-gate is not needed for controlling regions other than ones covered by local gate. The essential part of the device is shown in dashed boxes, where the Klein tunneling effect near GPNJs dominates in (b, c, d). (e) Gate biasing scheme for ON and OFF state. Gray region corresponds to the energy range of the transmission gap in the ON state. (f) Equivalent small signal circuit.

2 Methods

Klein tunneling across a graphene p-n junction is driven by the conservation of pseudospin, which in turn is set by the phase coherent superposition of the dimer p_z basis sets. The GPNJ acts as an efficient momentum filter, transmitting electrons that are injecting perpendicularly to the junction regardless of the barrier height across the junction. A GPNJ with a graded junction potential further filters the non-normal electrons aggressively, as those electrons see an angle dependent tunnel barrier akin to the cut-off modes in a rectangular waveguide^{28,30}. The device considered in this work contains two back-to-back GPNJs controlled by two gates including a trapezoidal gate and a back gate, as shown in Fig.1. (a). The GPNJ on the right has a tilted angle $\delta(= \pi/4)$ with respect to the left one¹⁷. In the OFF state, n-p-n regions are formed in the channel by applying proper gate biasing. These two back-to-back p-n junctions will collectively turn off the current. The left GPNJ serves as a collimator which blocks most of the incoming electrons except for those incident perpendicular to it; the second tilted GPNJ further blocks the electrons coming from the collimator allowing in turn only electrons perpendicular to itself to pass. OFF state is thereby achieved through sequential momentum filtering when the angle of the second junction exceeds the critical angle at the first junction. The average gate length considered in this work is $1 \mu\text{m}$ with a split length of $d_{1,2}=80 \text{ nm}$. For this paper, we assume a gate oxide with an equivalent SiO_2 thickness of 5 nm ($\text{EOT}=5 \text{ nm}$). In the ON state, the three regions in the graphene channel are held as n-n-n, so there is no angular filtering of electrons in the Fermi window between μ_S and μ_D for low V_{DS} . Filtering exists for portion of energy window (transmission gap shown in Fig. 2b) which comes into act for high V_{DS} . The small transmission gap exists due to slight differential doping (n-p-n). This leads to current saturation in the ON state. In the OFF state, we move the polarity of the central gate to n-p-n where the gap increases substantially and the current drops.

It should be noted that the GKTFET proposed here is designed to establish proof-of-concept. In practice the geometry needs to be optimized keeping in mind the fabrication techniques, considering different approaches such as electrical gating (Fig.1 (b)) or contact-induced doping³¹/chemical doping (Fig.1 (c))^{32,33} to create the side gated regions (blue n-doped regions in Fig.1 (a)). According to our finite element electrostatic calculations using Ansoft Maxwell, the side gate in (Fig.1 (b)) at the drain end (back gate) introduces a large parasitic capacitance. This extra capacitance will possibly compromise the cut-off frequencies if it is AC connected to the ground directly. Extra care should be taken to get rid of the effect of this capacitance, as we discuss later in this paper. Compared with electrostatic side gate doping, the chemical doping shown in Fig.1 (c) does not suffer from these large gate capacitances. However chemically doped graphene has lower carrier mobility. In Fig.1, we showed a proposed device with buried gates that was the basis for the calculations in this paper ; however, it is worth looking at alternate geometries, such as top gates^{11,34}, with the associated design trade-offs.

In our proposed device, the total current I_{DS} across the GKTFET can be estimated by the Landauer equation.

$$I_{DS} = \frac{2q}{h} \int T_{av} M [f(\mu_S) - f(\mu_D)] dE \quad (1)$$

where M is the number of modes, T_{av} is their mode-averaged transmission, q is the charge of the electron, h is the Planck's constant, f is the Fermi-Dirac distribution, and $\mu_{S,D}$ are the bias-separated electrochemical potentials in the source and drain. The mode-averaged transmission T_{av} and number of modes M at energy E are controlled by the potential drops on the channel V_{GS} . The resulting transconductance g_m can be written as

$$g_m = \frac{\partial I_{DS}}{\partial V_{GS}} \propto \int \frac{\partial (T_{av} M)}{\partial V_{GS}} [f(\mu_S) - f(\mu_D)] dE \quad (2)$$

$$\approx T_{av} M \Big|_{\mu_S}^{\mu_D} \quad (3)$$

In the ON state, the GKTFET has a small transmission gap around the Dirac point so that its mobility and g_m are expected to resemble a pristine GFET with the same dimensions. The presence of a transmission gap will, however, cause the current to saturate when the drain electrochemical potential μ_D moves towards the Dirac point and enters the transmission gap. In contrast, the g_m of ultra-clean GFETs has just a single point saturation precisely when μ_D hits the Dirac point since there is no gap in pristine graphene. This feature can be seen later in Fig.3. The output resistance r_{out} can be estimated by

$$r_0 = \frac{\partial V_{DS}}{\partial I_{DS}} \propto \left(\int M T_{av} \frac{\partial f(\mu_D)}{\partial \mu} dE \right)^{-1} \quad (4)$$

From eq (4), it can be seen that the output resistance depends on the modes inside the band gap in quasi-ballistic limit. A perfect energy gap in principle leads to infinite output resistance because $M T_{av} = 0$ in the gap, while any states inside the gap due to imperfections (such as scattering, defects) will lead to a finite output resistance. In our proposed devices, the output resistance is limited primarily by the edge reflection and carrier scattering.

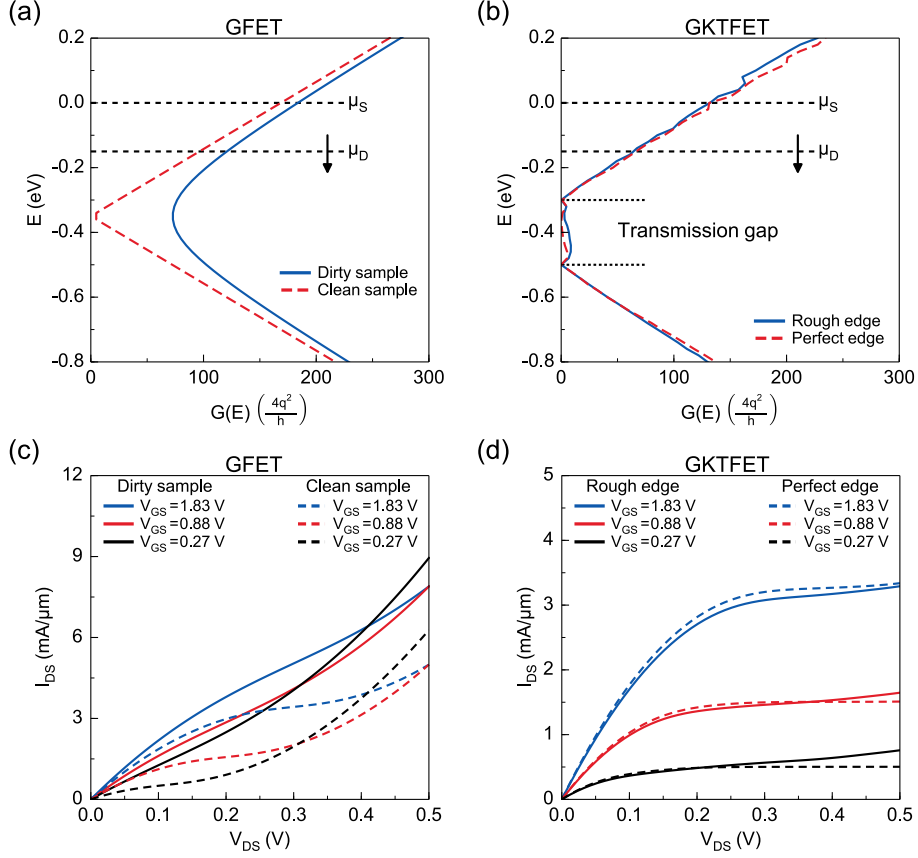


Figure 2. Conductance and output characteristics. (a) Energy resolved conductance for GFET (on-state). $G(E) \propto |E|$ corresponds to the Dirac cone-like band structure of clean sample (dash), and $G(E) \propto \sqrt{E^2 + 2\sigma^2/\pi}$ in dirty sample (solid)³⁵. (b) Energy resolved conductance for GKTFET (on-state). A clear transmission gap can be observed unlike GFET in (a). $G(E)$ in the transmission gap is slightly non-zero due to the edge reflections even with the perfect edge. Adding edge roughness creates more states inside the transmission gap. (c) I_{DS} vs. V_{DS} for GFET. I_{DS} in dirty graphene sample (solid) is a linear function of V_{DS} whereas clean graphene sample (dash) shows one point saturation. (d) I_{DS} vs. V_{DS} for GKTFET. GKTFET shows obvious current saturation in both cases with (solid) and without (dash) edge roughness. With edge roughness, it shows slightly larger slope in the saturation region which in turn reduces r_{out} due to increment of states inside the transmission gap. Gate voltages are calculated considering quantum capacitance where 0.3 V, 0.2 V, and 0.1 V are dropped in channel respectively for gate voltages mentioned both in (c) and (d).

In this work, we simulate the GKTFET using a semiclassical ray-tracing method coupled with analytical equations for chiral tunneling across the junctions²⁸. Standard quantum transport methods like the non-equilibrium Green's function formalism (NEGF)^{35,36}, are computationally quite expensive for GKTFETs with sizes between few hundreds of nanometers to micro-meters, and moreover, bring in spurious interference effects that are irrelevant at room temperature. In contrast, the ray-tracing method³⁷⁻³⁹ coupled with a well-benchmarked quantum tunneling model across junctions can be applied readily to devices at high voltage bias with large areas and complicated geometries including a sequence of multiple reflections, and has shown excellent agreement with recent experiments on GPNJs²⁸. In our approach, electrons are thrown from the source randomly with injection angles following a cosine distribution (the angular distribution of the quantized transverse wave-vectors). The average transmission (T_{av}) across the junctions is then calculated by counting electrons that successfully reach the drain. The analytical transmission probability for each electron across the junction is a simple generalization of Gaussian filtering $T \sim \exp^{-\pi k_F (d/2) \sin^2 \theta}$ established in³⁰ and extended now to an asymmetrically doped junction¹⁷. Here, d is the split length of the junction, θ is the incident angle of the electron, and k_F is the Fermi vector on both sides.

In our calculations, we considered the cases of GPNJ with perfect edges as well as rough edges. Fig. 2 shows the integrated transmission of (a) bulk graphene and (b) GKTFET, both for clean vs. dirty sample (charge puddles for bulk and edge roughness for GKTFETs). We see that pristine graphene has no band gap and its density of states $D(E) \propto |E|$ for a clean

sample, while $D(E) \propto \sqrt{E^2 + 2\sigma^2/\pi}$ for a dirty sample³⁵, with $\sigma^2 \approx 2\hbar^2 v_F^2 n_{imp} + C$ describing the contribution of charge puddles in washing out the Dirac point through spatial averaging. We use a typical impurity density in a dirty sample with $n_{imp} = 1 \times 10^{12} \text{ cm}^{-2}$ in this work³⁵. In contrast with GFETs, GKTFETs have a distinct transmission gap, as indicated in Fig. 2 (b). Indeed, very few modes appear in the transmission gap. These gap states arise from edge reflection of electrons rejected by the second junction, a process that redirects them towards the drain. Ultimately these states contribute to the leakage current in the off-state and lead to a finite r_{out} . Our calculation indicates that perfect edges in the GKTFET can reduce the leakage current by 20 to 40 times compared with GKTFET with rough edges in a $1 \mu\text{m}$ wide device. In our calculation, the edge roughness introduces a random reflection angle with a variance of $\sigma = 18^\circ$.

3 Results

Fig. 2 (c) and (d) shows the $I_{DS}-V_{DS}$ characteristics of GFETs and GKTFETs. In each case, the dashed lines are for clean samples while the solid lines include imperfections. It can be seen clearly that an ultraclean GFET shows $I_{DS} - V_{DS}$ with single-point saturation, while a GFET with a dirty sample shows a quasi-linear $I_{DS} - V_{DS}$ due to spatial averaging that washes out the Dirac point. In contrast, GKTFETs with both perfect and rough edges show a clear current saturation due to the presence of a pseudogap. The rough edges in GKTFETs lead to only a marginally smaller r_{out} because of the increase of MT_{av} in the transmission gap, which can be understood using eq.(4).

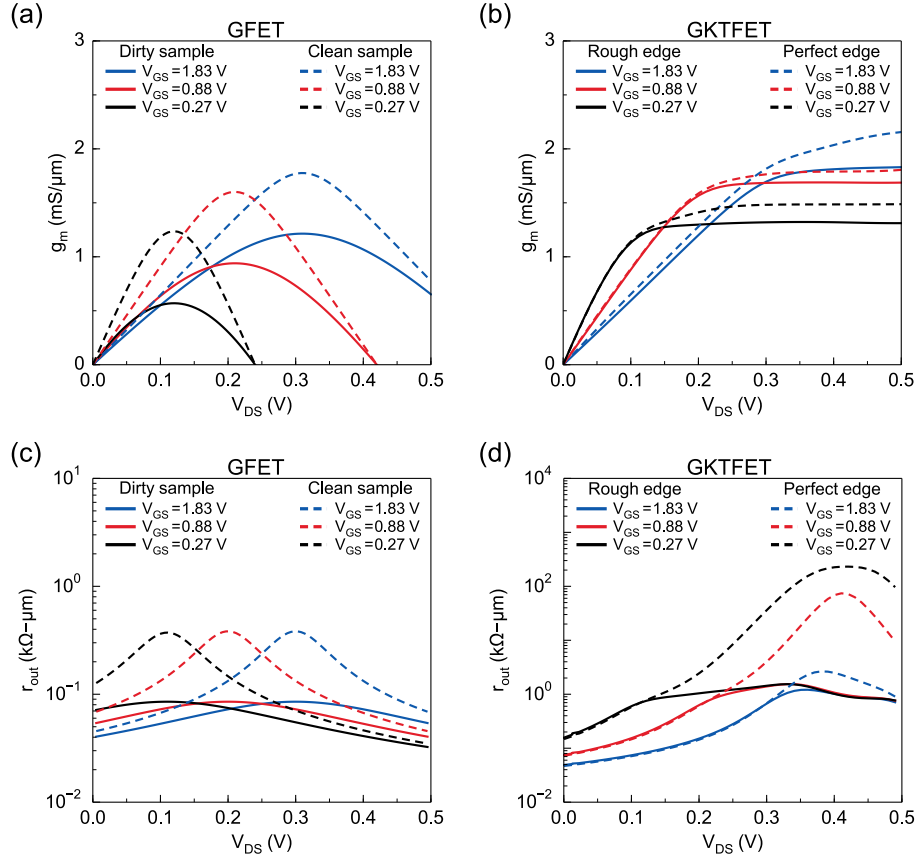


Figure 3. Transconductance (g_m) and output resistance (r_{out}) for GFET and GKTFET. (a) g_m vs. V_{DS} in GFET for dirty (solid) and clean (dash) sample where g_m is between 0.5 to 1.5 $\text{mS}/\mu\text{m}$ at saturation points. (b) g_m vs. V_{DS} in GKTFET with (solid) and without (dash) edge roughness where effect of edge roughness is not significant on g_m . (c) r_{out} vs. V_{DS} in GFET for dirty (solid) and clean (dash) sample where r_{out} is found to be around 0.1 $\text{k}\Omega\text{-}\mu\text{m}$ for dirty sample. (d) r_{out} vs. V_{DS} in GKTFET with (solid) and without (dash) edge roughness. Although r_{out} in GKTFET reduces from 10-100 $\text{k}\Omega\text{-}\mu\text{m}$ to about 1 $\text{k}\Omega\text{-}\mu\text{m}$ due to edge roughness, still in both cases, output resistances (r_{out}) are greater than the ones for GFET in (c) utilizing transmission gap.

Fig. 3 show the g_m and r_{out} of GFET and GKTFETs. The g_m of GFETs reach 0.5 to 1.5 $\text{mS}/\mu\text{m}$ (each gated region is $1 \mu\text{m}$ long in our simulation with linear transition length of 80 nm (split length, d) each), while the GKTFET turns out

to have a slightly higher g_m of 1 to 2 mS/ μm . The output characteristic however proves more dramatic than the transfer characteristic. The GFET shows a very low r_{out} of 0.1 k Ω - μm for dirty samples, and only around $r_{out} \sim 0.3$ k Ω - μm for clean samples at saturation V_{DS} for all gate biases, dropping rapidly for other V_{DS} values. At zero temperature, $\frac{\partial f(\mu_2)}{\partial \mu_2} = \delta(E - \mu_2)$ in eq (4), $r_{out} = \infty$ as $MT_{av} = 0$ at the Dirac point. At finite temperature r_{out} drops to a finite value because $\frac{\partial f(\mu_2)}{\partial \mu_2}$ has a non-vanishing spread of kT . Compared with GFETs, the GKTFET shows much higher r_{out} of 1 k Ω - μm even with edge roughness. GKTFET with perfect edges shows even higher r_{out} values that can reach 50 to 100 k Ω - μm . Furthermore, the saturation region corresponds to a V_{DS} in the range of 0.1 to 0.3 V instead of one point saturation.

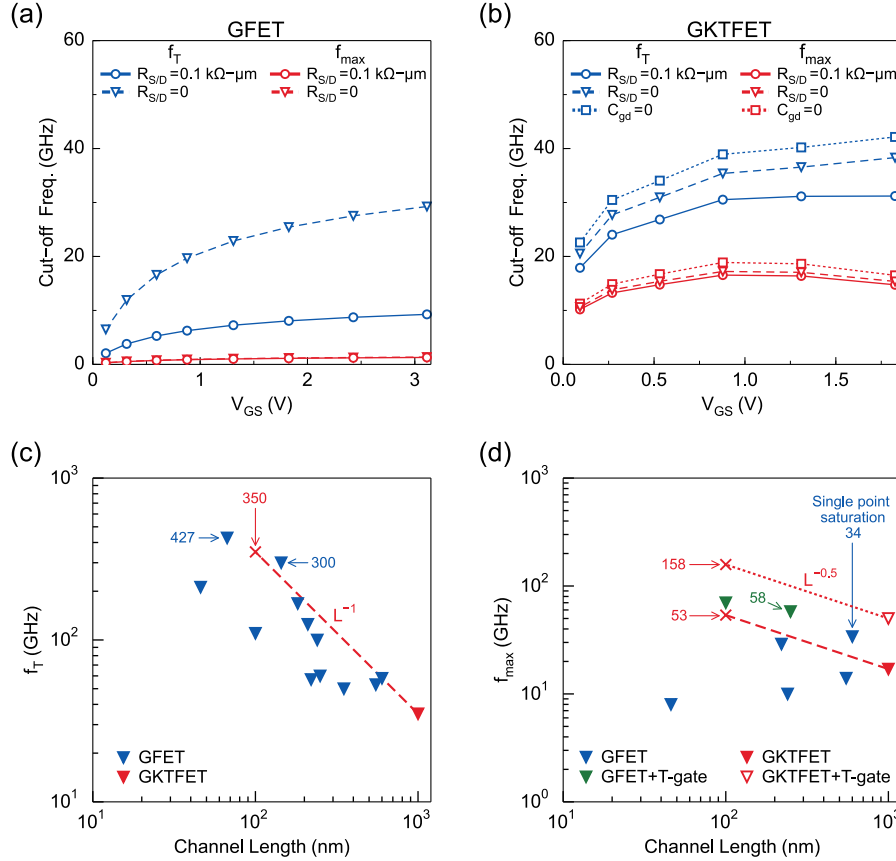


Figure 4. Cut-off frequencies for GFET and GKTFET. (a) f_T and f_{max} for GFET. The f_{max} of GFET is significantly smaller than f_T because of the small r_{out} . (b) f_T and f_{max} for GKTFET. f_T and f_{max} of GKTFET reach their maximum at the saturation region which range over 0.1 V to 0.3 V. Due to high output resistance, the max f_{max} in GKTFETs is about 50% of the maximum f_T . (c) f_T vs. channel length of GKTFET compared to reported GFETs. (d) f_{max} vs. channel length of GKTFET compared to reported GFETs. GFETs' data are from Ref. 10,11,34,40-42. Reported f_T s of GFETs are roughly inversely proportional to channel length, while the f_{max} s do not show this trend due to low output resistance. For ideally scaled GKTFET with 100 nm channel length, f_T is expected to reach 350 GHz (shown by red cross in (c)), which is comparable to the highest reported f_T s in GFETs (mentioned in the figure). The scaling of f_{max} of GKTFET follows $L^{-0.5}$ ideally. For a GKTFET with 100 nm channel, the f_{max} is expected to reach 53 GHz, and even high f_{max} =158 GHz can be expected if T-gate technique is used to reduce gate resistance (both shown by red cross in (d)).

To estimate the RF properties such as f_T and f_{max} of graphene-based RF devices, we consider the equivalent circuit for AC signals, shown in Fig.1 (e). This structure assumes that the dominant capacitance is from the central gate that is swung between p and n polarities, while the side gated regions have lower capacitance (we discuss this point later in the paper) For this equivalent circuit, the f_T and f_{max} can be estimated by⁴³.

$$f_T = \frac{g_m}{2\pi(C_{gs} + C_{gd})} \frac{1}{\sqrt{[1 + g_0(R_S + R_D)]^2 - (g_0 R_S)^2}} \quad (5)$$

with $g_0 = g_{ds} + g_m [C_{gd}/(C_{gs} + C_{gd})]$ and

$$f_{max} = \frac{f_T}{2\sqrt{\frac{R_G + R_S}{r_{ds}} + 2\pi f_T R_G C_{gd}}}. \quad (6)$$

To illustrate the impact on f_T and f_{max} from improved g_m and r_{out} of GKTFET in comparison with GFETs, we use $C_{gs}=6.9$ pF/mm, $C_{gd}=0.7$ pF/mm and $R_G=1$ k Ω - μ m for both transistors. However, it is worth re-emphasizing that the parameters are strongly dependent on the device geometry, for instance, the C_{gd} of the GKTFET in Fig.1 (b) is in fact negligible by finite element electrostatic calculation using Ansoft Maxwell. We accordingly choose an experimentally achievable ratio of $C_{gd}/C_{gs}=0.1$ ¹¹ in the following calculations of f_T and f_{max} . It should be noted that our calculations for f_T and f_{max} using small C_{gd} are only valid for saturation region.

Fig. 4 show the peak value of f_T and f_{max} of the GFET and GKTFET. The f_T reaches 9.3 to 29.3 GHz in GFETs with a channel length of $L_{channel}=1$ μ m (better contact resistances and smaller C_{gd} gives higher f_T). It is known that the f_T in pristine GFETs is inversely proportional to $L_{channel}$ ⁴³. Projecting accordingly, a channel length of 100 nm leads to an expected max $f_T=100$ to 300 GHz for a conventional GFET, which agrees with the published literature^{10,11,34,40-42}. The f_{max} of the GFET reaches only 1.3 GHz, i.e., 14% of f_T because of its small output resistance. Compared with the ideal case where $R_{S/D}=0$, the f_{max} of GFET with larger $R_{S/D}=0.1$ k Ω - μ m is reduced by 5%, while the peak f_T is reduced by 69%.

Compared with GFETs, the f_T of the GKTFET is larger due to a larger g_m arising from the opening of the transport gap and the resulting variation in density of states over the finite temperature window. More noticeably, the f_{max} and f_{max}/f_T ratio in GKTFET are significantly higher due to the current saturation arising from the engineered pseudogap. Fig. 4 (b) and (e) show that the GKTFET with 1 μ m channel length reaches a f_T of 31 GHz and f_{max} of 17 GHz. The f_{max} is 13 times larger than that of GFET. Furthermore, the contact resistance has a much weaker impact on f_T in GKTFET - in fact, 0.1 k Ω - μ m R_S and R_D reduces the f_T by only ~ 10 -20%. The impact of R_S and R_D to f_T in both GFETs and GKTFET is determined by the factor $g_{ds}(R_S + R_D)$, $g_{ds} = 1/r_{out}$, as we see in the denominator of equation (5). The large output resistance r_{out} of GKTFET weakens the influence of R_S and R_D on the f_T . In Fig.4, we also show the f_T and f_{max} in the limit of $C_{gd}=0$ by the dashed lines. It can be seen that the small C_{gd} leads to a 30% increase of the max f_T and 10% increase of max f_{max} .

4 Discussion

We have shown that a 1 μ m long GKTFET shows much better r_{out} and cutoff frequencies f_{max} than GFETs due to the transmission gap engineered in pristine graphene using gate geometry. Perfect edges in a GKTFET would further reduce the leaked density of states in the transmission gap, leading to larger r_{out} and f_{max} . The small contact resistances R_S/R_D also have significant impacts to the cut off frequency f_T as they compete with r_{out} . Compared with GFET, the f_T of the GKTFET is less sensitive to R_S and R_D due to a larger r_{out} .

The parasitic capacitances C_{gd} and gate resistance R_G are critical device parameters and significantly impact f_T and f_{max} . The C_{gd} and R_G are strongly dependent on the real design and geometry of the transistor. For instance, recent experiments used T-shape gate to reduce R_G dramatically to get high f_{max} in GFETs¹¹. Simply including a sizeable side gate would create a large parasitic capacitance AC connected to the ground. To mitigate this, we will need to reference the third gate to the drain at a constant bias offset or include an inductor between the two to filter out the high-frequency AC signals. A more convenient choice would be to dope the two end regions chemically and work with a trapezoidal central gated region alone.

While our simulations were done for 1 μ m, the ultimate advantage of the GKTFET for high-performance RF depends on its overall scalability, since the C_{gs} and R_G^{-1} are proportional to the channel length. In the GKTFET, the gate width and length are related, as we used a 45 $^\circ$ tilted Junction. We show the f_T and f_{max} of GKTFETs and GFETs in Fig.4. Ideally, the f_T and f_{max} follow $f_T \propto C_{gs}^{-1} \propto L^{-1}$ and $f_{max} \propto C_{gs}^{-1} R_G^{-0.5} \propto L^{-0.5}$. The scaling of the gate length of the GKTFET with from 1 μ m to 100 nm is expected to increase the f_T and f_{max} by 10 and 3.2 times respectively, as indicated by the dashed lines. In contrast, the f_{max} of GFETs does not scale with channel length due to the low output resistance, as shown in Fig.4 (f). To estimate the f_T and f_{max} of 100 nm GKTFETs, we made the following assumptions: the scaling down of the GKTFET does not change the electrostatics in the device (gate control is still dominant), the pseudogap can be effectively created by GPNJs in a scaled GKTFET, and device parameters such as C_{gs} and C_{gd} scale properly with channel length while maintaining the transition length (split length, d) across junctions in the range of 50-100 nm for better electron filtering resulting in transmission gap. Detailed quantum simulations coupled with numerical 3D electrostatics are needed to test the performance of these devices at their scaling limits. Trap charges, edge roughness, junction roughness, and contact resistance are important factors that will affect RF performances of realistic devices, therefore, those variabilities in real devices should be carefully calibrated⁴⁴. In principle these non-idealities can be mitigated using hBN substrates, gated edges, graphite gates, and 1D metal edge contacts (contact resistance ~ 150 Ω - μ m⁴⁵) which will be explored in future publications.

5 Conclusion

To summarize, we propose a conceptual high-frequency RF device in Fig.1. This device operates by geometry engineering of a gate-tunable transport gap in pristine graphene, using the physics of Klein tunneling. In contrast to conventional GFETs which suffer from weak current saturation due to gaplessness, the engineering of a transmission gap allows the GKTFET to enjoy both high carrier lifetimes and current saturation. Our calculation of the GKTFET shows a significant improvement on f_{max} and a slightly higher f_T compared with GFETs. The device is expected to achieve an f_T of 33 GHz and a comparable f_{max} of 17 GHz in a device with 1 μm gate length, and ramp up to $f_T=350$ GHz and $f_{max}=53$ GHz as we shrink the gate to 100 nm. Higher f_{max} of 49 GHz for 1 μm channel and 158 GHz for 100 nm channel can be expected by reducing gate resistance with the technique of T-Gate. In addition, the cut-off frequencies of the GKTFET are seen to be much less sensitive to the contact resistance than GFETs, once again due to the significant increase in output resistance arising from current saturation.

References

1. Schwierz, F. Graphene transistors. *Nat. nanotechnology* **5**, 487–496 (2010).
2. Schwierz, F. Graphene transistors: status, prospects, and problems. *Proc. IEEE* **101**, 1567–1584 (2013).
3. Fiori, G. *et al.* Electronics based on two-dimensional materials. *Nat. nanotechnology* **9**, 768–779 (2014).
4. Chauhan, J. & Guo, J. Assessment of high-frequency performance limits of graphene field-effect transistors. *Nano Res.* **4**, 571–579 (2011).
5. Bolotin, K. I. *et al.* Ultrahigh electron mobility in suspended graphene. *Solid State Commun.* **146**, 351–355 (2008).
6. Chen, J.-H., Jang, C., Xiao, S., Ishigami, M. & Fuhrer, M. S. Intrinsic and extrinsic performance limits of graphene devices on SiO_2 . *Nat. nanotechnology* **3**, 206–209 (2008).
7. Dean, C. R. *et al.* Boron nitride substrates for high-quality graphene electronics. *Nat. nanotechnology* **5**, 722–726 (2010).
8. Morozov, S. *et al.* Giant intrinsic carrier mobilities in graphene and its bilayer. *Phys. review letters* **100**, 016602 (2008).
9. Wu, Y. *et al.* State-of-the-art graphene high-frequency electronics. *Nano letters* **12**, 3062–3067 (2012).
10. Cheng, R. *et al.* High-frequency self-aligned graphene transistors with transferred gate stacks. *Proc. Natl. Acad. Sci.* **109**, 11588–11592 (2012).
11. Guo, Z. *et al.* Record maximum oscillation frequency in c-face epitaxial graphene transistors. *Nano letters* **13**, 942–947 (2013).
12. Ni, Z. H. *et al.* Uniaxial strain on graphene: Raman spectroscopy study and band-gap opening. *ACS nano* **2**, 2301–2305 (2008).
13. Han, M. Y., Özyilmaz, B., Zhang, Y. & Kim, P. Energy band-gap engineering of graphene nanoribbons. *Phys. review letters* **98**, 206805 (2007).
14. Perebeinos, V. & Avouris, P. Inelastic scattering and current saturation in graphene. *Phys. Rev. B* **81**, 195442 (2010).
15. Meric, I., Baklitskaya, N., Kim, P. & Shepard, K. L. Rf performance of top-gated, zero-bandgap graphene field-effect transistors. In *Electron Devices Meeting, 2008. IEDM 2008. IEEE International*, 1–4 (IEEE, 2008).
16. Sajjad, R. N. & Ghosh, A. W. High efficiency switching using graphene based electron optics. *Appl. Phys. Lett.* **99**, 123101 (2011).
17. Sajjad, R. N. & Ghosh, A. W. Manipulating chiral transmission by gate geometry: switching in graphene with transmission gaps. *ACS nano* **7**, 9808–9813 (2013).
18. Beenakker, C. Colloquium: Andreev reflection and Klein tunneling in graphene. *Rev. Mod. Phys.* **80**, 1337 (2008).
19. Allain, P. E. & Fuchs, J. Klein tunneling in graphene: optics with massless electrons. *The Eur. Phys. J. B-Condensed Matter Complex Syst.* **83**, 301–317 (2011).
20. Katsnelson, M., Novoselov, K. & Geim, A. Chiral tunnelling and the Klein paradox in graphene. *Nat. physics* **2**, 620–625 (2006).
21. Low, T., Hong, S., Appenzeller, J., Datta, S. & Lundstrom, M. S. Conductance asymmetry of graphene pn junction. *IEEE Transactions on Electron Devices* **56**, 1292–1299 (2009).
22. Sajjad, R. N., Sutar, S., Lee, J. & Ghosh, A. W. Manifestation of chiral tunneling at a tilted graphene p-n junction. *Phys. Rev. B* **86**, 155412 (2012).

23. Sutar, S. *et al.* Angle-dependent carrier transmission in graphene p–n junctions. *Nano letters* **12**, 4460–4464 (2012).
24. Elahi, M. M. & Ghosh, A. W. Current saturation and steep switching in graphene pn junctions using angle-dependent scattering. In *Device Research Conference (DRC), 2016 74th Annual*, 1–2 (IEEE, 2016).
25. Jang, M. S., Kim, H., Son, Y.-W., Atwater, H. A. & Goddard, W. A. Graphene field effect transistor without an energy gap. *Proc. Natl. Acad. Sci.* **110**, 8786–8789 (2013).
26. Wilmart, Q. *et al.* A klein-tunneling transistor with ballistic graphene. *2D Mater.* **1**, 011006 (2014).
27. Morikawa, S. *et al.* Dirac fermion reflector by ballistic graphene sawtooth-shaped npn junctions. *Semicond. Sci. Technol.* **32**, 045010 (2017).
28. Chen, S. *et al.* Electron optics with pn junctions in ballistic graphene. *Sci.* **353**, 1522–1525 (2016).
29. Supplementary Information.
30. Cheianov, V. V. & Fal’ko, V. I. Selective transmission of dirac electrons and ballistic magnetoresistance of n- p junctions in graphene. *Phys. review b* **74**, 041403 (2006).
31. Cayssol, J., Huard, B. & Goldhaber-Gordon, D. Contact resistance and shot noise in graphene transistors. *Phys. Rev. B* **79**, 075428 (2009).
32. Brenner, K. & Murali, R. Single step, complementary doping of graphene. *Appl. Phys. Lett.* **96**, 063104 (2010).
33. Tang, B., Guoxin, H. & Gao, H. Raman spectroscopic characterization of graphene. *Appl. Spectrosc. Rev.* **45**, 369–407 (2010).
34. Liao, L. *et al.* High-speed graphene transistors with a self-aligned nanowire gate. *Nat.* **467**, 305–308 (2010).
35. Sajjad, R. N., Tseng, F., Habib, K. M. & Ghosh, A. W. Quantum transport at the dirac point: Mapping out the minimum conductivity from pristine to disordered graphene. *Phys. Rev. B* **92**, 205408 (2015).
36. Sajjad, R. N., Polanco, C. A. & Ghosh, A. W. Atomistic deconstruction of current flow in graphene based hetero-junctions. *J. Comput. Electron.* **12**, 232–247 (2013).
37. Beenakker, C. & Van Houten, H. Billiard model of a ballistic multiprobe conductor. *Phys. review letters* **63**, 1857 (1989).
38. Milovanović, S., Ramezani Masir, M. & Peeters, F. Spectroscopy of snake states using a graphene hall bar. *Appl. Phys. Lett.* **103**, 233502 (2013).
39. Milovanović, S., Ramezani Masir, M. & Peeters, F. Magnetic electron focusing and tuning of the electron current with a pn-junction. *J. Appl. Phys.* **115**, 043719 (2014).
40. Lin, Y.-M. *et al.* Development of graphene fets for high frequency electronics. In *Electron Devices Meeting (IEDM), 2009 IEEE International*, 1–4 (IEEE, 2009).
41. Lin, Y.-M. *et al.* 100-ghz transistors from wafer-scale epitaxial graphene. *Sci.* **327**, 662–662 (2010).
42. Meric, I. *et al.* High-frequency performance of graphene field effect transistors with saturating iv-characteristics. In *Electron Devices Meeting (IEDM), 2011 IEEE International*, 2–1 (IEEE, 2011).
43. Rutherglen, C., Jain, D. & Burke, P. Nanotube electronics for radiofrequency applications. *Nat. Nanotechnol.* **4**, 811–819 (2009).
44. Xu, G., Zhang, Y., Duan, X., Balandin, A. A. & Wang, K. L. Variability effects in graphene: Challenges and opportunities for device engineering and applications. *Proc. IEEE* **101**, 1670–1688 (2013).
45. Wang, L. *et al.* One-dimensional electrical contact to a two-dimensional material. *Sci.* **342**, 614–617 (2013).
46. Champlain, J. G. A physics-based, small-signal model for graphene field effect transistors. *Solid-State Electron.* **67**, 53–62 (2012).

Acknowledgments

This work is supported in part by the Nanoelectronics Research Corporation (NERC), a wholly owned subsidiary of the Semiconductor Research Corporation (SRC), through the Institute for Nanoelectronics Discovery and Exploration (INDEX). The authors acknowledge computational resources on UVa HPC System Rivanna. We acknowledge Cory R. Dean from Columbia University, Kurt Gaskill from Naval Research Laboratory, Claire Berger from Georgia Institute of Technology and Philip Kim from Harvard University for helpful discussions.

Author contributions statement

Y. T. analyzed the device DC and RF characteristics and wrote the manuscript. M. E. performed the ray-tracing calculations for the current and wrote the manuscript. H. T. analyzed the device parasitic capacitors. K. H. and M. E. developed the ray-tracing code. N. B. and A. G. supervised the work. A. G. initialized the idea. All authors contributed to revising the manuscript.

Additional information

Competing financial interests: The authors declare no competing financial interests.